J|A|C|S
JOURNAL OF THE AMERICAN CHEMICAL SOCIETY
pubs.acs.org/JACS
Article

Oxygen Reduction Pathway for Spinel Metal Oxides in Alkaline Media: An Experimentally Supported Ab Initio Study

Colin R. Bundschu,* Mahdi Ahmadi, Juan F. Méndez-Valderrama, Yao Yang, Héctor D. Abruña,* and Tomás A. Arias*

Cite This: J. Am. Chem. Soc. 2024, 146, 4680−4686

Read Online

ACCESS | Metrics & More | Article Recommendations | SI Supporting Information

ABSTRACT: Precious-metal-free spinel oxide electrocatalysts are promising candidates for catalyzing the oxygen reduction reaction (ORR) in alkaline fuel cells. In this theory-driven study, we use joint density functional theory (JDFT) in tandem with supporting electrochemical measurements to identify a novel theoretical pathway for the ORR on cubic Co_3O_4 nanoparticle electrocatalysts, which aligns more closely with experimental results than previous models. The new pathway employs the cracked adsorbates *(OH)(O) and *(OH)(OH), which, through hydrogen bonding, induce spectator surface *H. This results in an onset potential closely matching experimental values, in stark contrast to the traditional ORR pathway, which keeps adsorbates intact and overestimates the onset potential by 0.7 V. Finally, we introduce electrochemical strain spectroscopy (ESS), a groundbreaking strain analysis technique. ESS combines ab initio calculations with experimental measurements to validate the proposed reaction pathways and pinpoint rate-limiting steps.

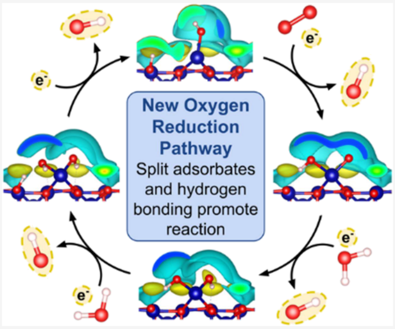

1. INTRODUCTION

The high cost of platinum alloys and the sluggish kinetics of the oxygen reduction reaction (ORR) at the cathode present major hurdles to the commercialization of both acidic and alkaline fuel cells.[1−6] Great attention has been devoted to finding nonprecious metal electrocatalysts that could resolve these issues. In this search, metal−nitrogen doped carbons (M−N/C),[7] spinel oxides (Co, Mn, Fe),[8−10] and perovskites[11] are of considerable interest in alkaline fuel cells due to their faster ORR kinetics and high stability in alkaline environments.[12]

In the case of spinel oxides, numerous strategies have been attempted to optimize the reactivity and stability of catalysts for the ORR. Xiong et al. found that in a Mn-doped cobalt ferrite, a synergistic effect between Co and Mn enhances the ORR reactivity while Fe stabilizes the catalyst by preserving the spinel structure.[8] Wei et al. explored the effect of Mn valency on activity and found that the ORR activity of $MnCo_2O_4$ produces a volcano shape as a function of the Mn valence state, peaking at a valence of +3.[13] Li et al. showed that the crystalline structure of spinel $CoMn_2O_4$ affects its reactivity, with higher activity in cubic $CoMn_2O_4$ than in tetragonal $CoMn_2O_4$.[14] Of the numerous parameters, the shape and structure of nanoparticle (NP) facets, in particular, strongly affect ORR performance.[15−17] For example, it was found that ellipsoidal Mn_3O_4 NPs achieve higher ORR activity than spherical and cubic NPs,[9] while Gao et al. showed that $Co_3O_4(111)$ exhibits a lower activation barrier for O_2 desorption when compared to $Co_3O_4(100)$, for the oxygen evolution reaction (OER).[16]

In contrast to these numerous experimental studies focused on improving ORR metal-oxide performance, attempts to elucidate the measured activity using ab initio calculations have proved consistently challenging.[18,19] Traditionally, the metal oxide alkaline ORR pathway has been believed to be *OH → *OO → *OOH → *O → *OH.[20] However, when tested using the simple (100) facet of Co_3O_4, this traditional pathway produces energies in disagreement with the experiment. Specifically, we demonstrate through joint density-functional theory (JDFT) calculations that the traditional pathway for the oxygen reduction reaction (ORR) on the $Co_3O_4(100)$ facet, computed at the experimental onset potential (V_{on}) we measure below and as previously observed in cyclic voltammetry experiments,[21] results in unphysical reaction barriers exceeding 0.7 eV. Furthermore, the most favorable path identified still requires kinetically challenging hopping of intermediates between surface sites.

Given the large discrepancies between the computed and experimental energies for the simple $Co_3O_4(100)$ test case, the traditional pathway very likely misses key reaction intermedi-

Received: October 26, 2023
Revised: January 17, 2024
Accepted: January 19, 2024
Published: February 7, 2024

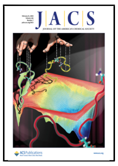

https://doi.org/10.1021/jacs.3c11977
J. Am. Chem. Soc. 2024, 146, 4680−4686

ates. Using the traditionally assumed pathway as a starting point, and drawing inspiration from known catalytic kinetics of platinum group metals (PGMs), we performed new JDFT calculations and propose that a more accurate alkaline ORR pathway on the $Co_3O_4(100)$ surface is

$$\begin{aligned}
&\mathbf{{}^*H + {}^*OH + 2H_2O + O_2 + 4e^-}\\
&\quad \rightarrow {}^*+{}^*(OH)(O) + 2H_2O + OH^- + 3e^-\\
&{}^*+{}^*(OH)(O) + 2H_2O + OH^- + 3e^-\\
&\quad \rightarrow {}^*+{}^*(OH)(OH) + H_2O + 2OH^- + 2e^-\\
&{}^*+{}^*(OH)(OH) + H_2O + 2OH^- + 2e^-\\
&\quad \rightarrow {}^*H + {}^*(OH)(OH) + 3OH^- + e^-\\
&{}^*H + {}^*(OH)(OH) + 3OH^- + e^-\\
&\quad \rightarrow \mathbf{{}^*H + {}^*OH + 4OH^-} \qquad (1)
\end{aligned}$$

as presented in Figure 1. As would be expected of the correct pathway, and unlike the traditional pathway, this pathway follows the minimum energy path (MEP) and "turns on", i.e., first presents no energy barrier, at the experimentally observed onset potential. Additionally, the new pathway appears to be kinetically feasible with all intermediates remaining on a single site. Finally, we use this pathway to demonstrate below that the ORR activity of cubic Co_3O_4 nanoparticles can be significantly tuned by controlling the nanoparticle strain.

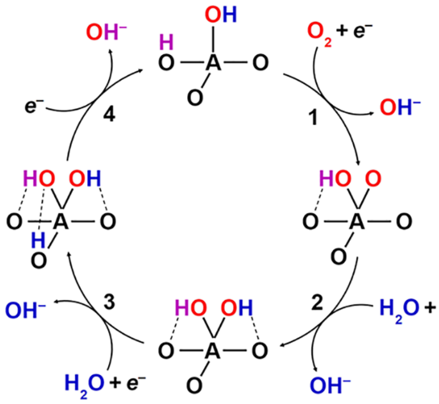

Figure 1. Schematic of the proposed, JDFT-identified ORR pathway/mechanism with colors differentiating adsorbed O (red), adsorbed H (blue), active spectator H (purple), and the Co^{2+} A-site with participating adjacent surface O sites (black). In step 4, the blue, surface-adsorbed H is equivalent by symmetry to the purple spectator H in the subsequent state so that the reaction can proceed without the need for the reactant to change the adsorption site.

2. RESULTS

2.1. Experimental Cubic Co_3O_4 Nanoparticle Characterization.

To test our ab initio predictions for the alkaline ORR pathway, we synthesized and characterized cubic $Co_3O_4(100)$ nanoparticles (NPs). We focused on the (100) facet due to its singular presence in cubic NPs, facilitating a more precise comparison between our theoretical and experimental results than would be possible with multifaceted NPs. Figure 2a shows a TEM image and (b) shows a size histogram of the NPs, with an average size of 53 ± 16 nm. Figure 2c shows the XRD pattern for the NPs alongside the reference single-phase spinel Co_3O_4 (PDF 01-076-1802). Figure 2d shows an atomic resolution bright field STEM image of the NPs and (e) shows the corresponding Fourier transform. The FFT image can be indexed as the [110] zone axis, which we chose for imaging due to the thickness of cubic NPs along the (100) facet. Figure 2f shows the ORR polarization profile for the NPs acquired at a scan rate of 5 mV s^{-1} in 1 M KOH at 1600 rpm. At potentials higher than ~0.8 V vs RHE, the current is kinetically controlled, while at lower potentials (<0.7 V vs RHE), a diffusion-limited current density of −3.7 mA/cm^2 was reached at 1600 rpm, which matches well with the expected current density of −3.8 mA/cm^2 for a $4e^-$ ORR process at 1600 rpm in 1 M KOH.[21] Additionally, our onset potential of 0.89 V vs RHE for the cubic surface is in excellent agreement with that of Yang et al.,[21] defined in both cases as the potential yielding 5% of the maximum current. Further analysis of the reaction kinetics and electron transfer number is presented in Supporting Information S3.

2.2. Identifying the Reaction Pathway.

To compute the energies of reaction intermediates on $Co_3O_4(100)$, we employed the most energetically favorable surface termination under the experimental conditions of 298 K and atmospheric oxygen partial pressure as determined by Zasada et al.[22] The resulting surface exhibits two possible surface Co attachment sites: the protruding tetrahedral (Tet) Co^{2+} and the surface octahedral (Oct) Co^{3+} sites (see Figure 3a, which presents our ab initio results for the solvated, relaxed surface without adsorbates).

With the surface state established, we first consider the traditional $4e^-$ pathway for alkaline ORR on metal oxide surfaces,[20] indicating the start and end states with boldface.

$$\begin{aligned}
&\mathbf{{}^*OH + 2H_2O + O_2 + 4e^-}\\
&\quad \rightarrow {}^*OO + 2H_2O + OH^- + 3e^-\\
&{}^*OO + 2H_2O + OH^- + 3e^-\\
&\quad \rightarrow {}^*OOH + H_2O + 2OH^- + 2e^-\\
&{}^*OOH + H_2O + 2OH^- + 2e^-\\
&\quad \rightarrow {}^*O + H_2O + 3OH^- + e^-\\
&{}^*O + H_2O + 3OH^- + e^-\\
&\quad \rightarrow \mathbf{{}^*OH + 4OH^-} \qquad (2)
\end{aligned}$$

In our treatment of this pathway, we compute the energy of each possible intermediate state at both the Co^{2+} and Co^{3+} sites, in each case considering the potential impact of "spectator" species, which are atoms or molecules not consumed in the reaction but significantly influence the reaction kinetics. In particular, we pay close attention to the adsorption and desorption dynamics of spectator *H and *OH, finding that their presence, especially that of *H on surface O sites neighboring the active Co site, markedly lowers the reaction's energetics and influences the kinetics.

We display our ab initio configurations of the traditional pathway in the top two rows of Figure 3c, organized from left to right by the reaction step, displaying the lowest energy spectator configuration for each reaction intermediate. The first row displays the intermediates on the tetrahedral Co^{2+} site, and the second row displays the intermediates on the octahedral Co^{3+} site. Even with the most energetically favorable spectators, at the experimental onset potential (V_{on}) of 0.89 V vs RHE,[21] along the traditional pathway we

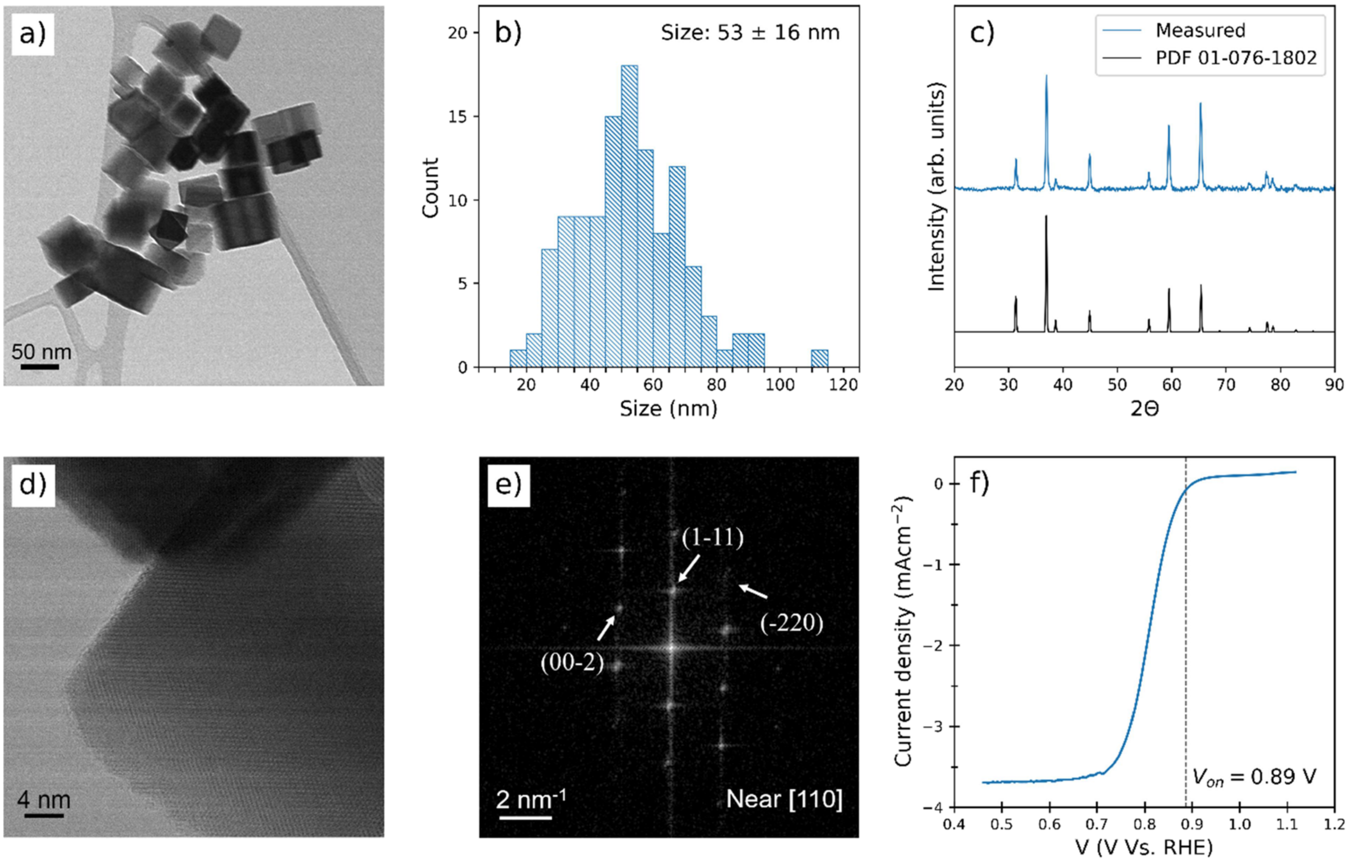

Figure 2. Characterization of cubic Co_3O_4 nanoparticles (NPs). (a) Representative TEM image. (b) Particle size distribution histogram. (c) Measured XRD patterns alongside reference single-phase spinel Co_3O_4 (PDF 01-076-1802). (d) High-resolution BF-STEM image and (e) corresponding Fourier transform. (f) ORR polarization profile in O_2-saturated 1.0 M KOH at 1600 rpm.

find a lower bound of 0.71 eV for the reaction barrier, coming from the *OH → *OO step (Figure 4a, upper, red pathway). Furthermore, this step requires the adsorbate to make a nontrivial transition from the Co^{2+} to the Co^{3+} site. Even if the kinetics associated with this transition were feasible, a barrier of this magnitude indicates that the reaction must occur along a different pathway.

To find a more energetically feasible pathway, we considered a richer set of adsorbed intermediates, which we present in rows 3−5 of Figure 3c, using the spectator configurations with the lowest energy. Inspired by the split configurations of PGM pathways,[23] we first investigated “cracked” configurations for the intermediates, i.e., those where the adsorbed O_2 remains bonded to a single Co site but the two O atoms are separated. We present these cracked configurations for the Co^{2+} site in row 3 of Figure 3c but do not present the cracked configurations for the Co^{3+} site as we found all such configurations spontaneously recombined. In addition to cracked configurations, we considered configurations involving the adsorbed O_2 “bridging” a Co^{2+} and a Co^{3+} site, presented in row 4, as well as configurations where a single O atom from the adsorbate is “shared” between two Co^{2+} and Co^{3+} sites, presented in row 5.

Many of the lowest energy configurations, including all of the cracked Co^{2+} configurations of row 3, feature an intermediate-stabilized spectator *H which plays a key role in reducing the total energy. For example, in all cases of row 3 except the *OH configuration, an adsorbed intermediate O hydrogen bonds to the spectator *H on a nearby surface O site, and this lowers the overall energy by as much as 1 eV. Additionally, in some of these O-stabilized configurations, the spectator *H lifts away from its surface O site and bonds more tightly with the adsorbed O, as in the configuration labeled * + *(OH)(O) (row 3, column 2). We denote this configuration as * + *(OH)(O), rather than *H + *(O)(O), to highlight the fact that the spectator *H sits closer to the adsorbed O than to its “home” surface at the O site. The kinetics of this rearrangement closely resemble the efficient proton transport of the Grotthuss mechanism[24] and provide a kinetically accessible alternative to the full hop between sites required by the traditionally assumed pathway.

At potentials near V_{on}, we find the cracked pathway on the Co^{2+} site with intermediates appearing along the “Tet Cracked” (row 3) of Figure 3

$$\begin{aligned} {}^*\mathrm{H} + {}^*\mathrm{OH} &\rightarrow {}^*+{}^*(\mathrm{OH})(\mathrm{O}) \\ &\rightarrow {}^*+{}^*(\mathrm{OH})(\mathrm{OH}) \\ &\rightarrow {}^*\mathrm{H} + {}^*(\mathrm{OH})(\mathrm{OH}) \\ &\rightarrow {}^*\mathrm{H} + {}^*(\mathrm{OH}) \end{aligned} \tag{3}$$

is the minimum energy pathway (MEP) for alkaline ORR on the $Co_3O_4(100)$ surface.

Figure 4a displays the free energies of the MEP configurations (black) alongside the energies of the traditional pathway (red) at our experimentally observed onset potential V_{on}. In correspondence with the experiment, the MEP, unlike the traditional pathway, presents no apparent barriers at V_{on}.

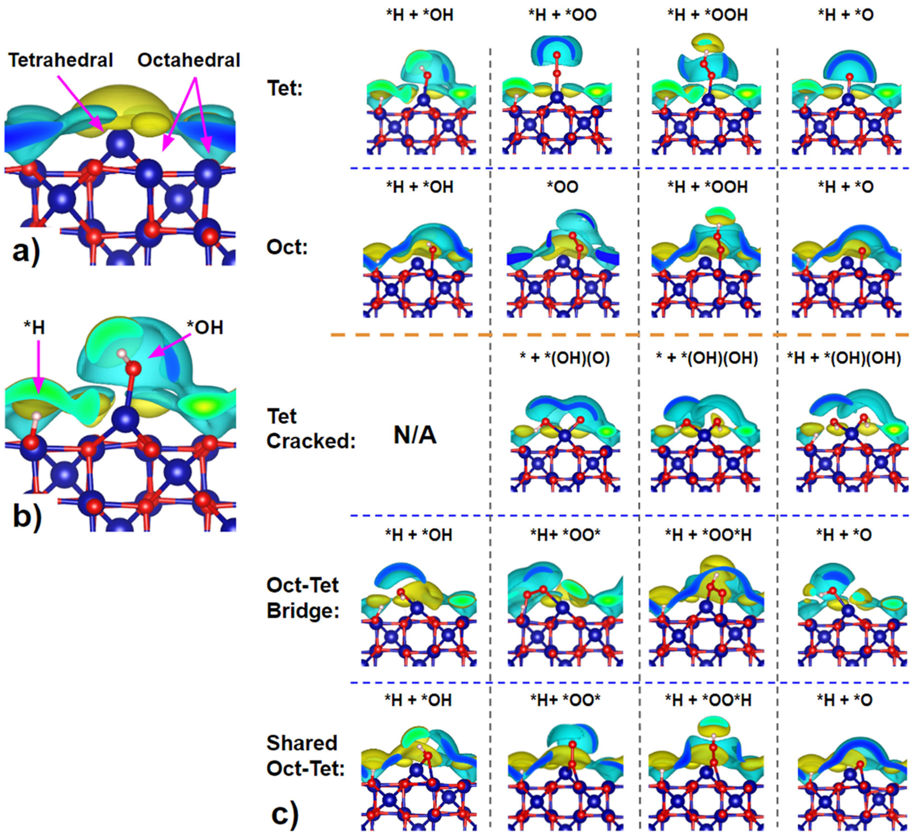

Figure 3. Solvated JDFT calculations of the (100) surface with (a) no adsorbates, (b) a spectator *H and an adsorbed *OH, and (c) adsorbates organized by the reaction step (columns) and adsorbate configuration (rows): Co atoms (blue), O atoms (red), H atoms (white), and positive and negative solvent-charge isosurfaces (blue/cyan and yellow surfaces, respectively). As expected, positive solvent charges (blue/cyan isosurfaces) surround the adsorbed and surface O atoms, whereas negative solvent charges (yellow) surround the adsorbed H and surface Co atoms (visualizations of the solvated surface generated using VESTA[25]).

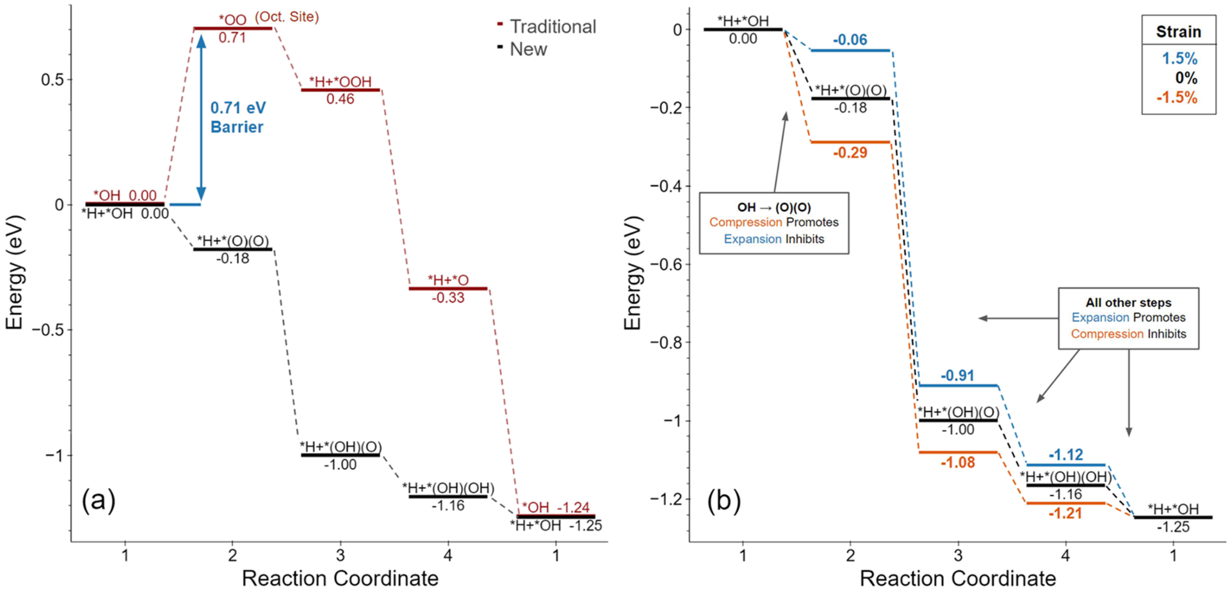

Figure 4. Reaction intermediate energies calculated for the (100) facet at our experimentally determined V_{on} = 0.89 V vs RHE, ordered by electron loss: (a) values for the best possible traditional pathway (upper, red levels) and the new proposed pathway (lower, black levels); (b) values along the proposed pathway at −1.5% (orange), 0% (black), and 1.5% (blue) tensile epitaxial strain. The reaction is cyclic, which we indicate by repeating step 1 in the figure at an energy separation corresponding precisely to the energy we calculate to be released in one cycle of the reaction.

Moreover, at the experimental onset potential, the MEP exhibits transition steps with very small energy drops, consistent with the reaction being near its onset. Additionally, this pathway gives insight into a potentially key rate-limiting step for the alkaline ORR on this surface. Specifically, V_{on} marks the point where it becomes energetically favorable for the adsorbed *OH to induce the spectator *H, which is necessary to eliminate barriers along the MEP. This suggests that the reaction onset is limited not only by the transition between any two steps in the reaction pathway but also by the ability to populate all necessary spectator states over competing alternatives.

2.3. Optimality of the New Reaction Pathway. To establish that our identified pathway in Equation 3 is indeed the most energetically favorable pathway, we combine our theoretical and experimental results as follows.

First, the simplicity of State 1, the *OH state, allowed us to conduct a comprehensive search of possible configurations for this state, including those with *H and *OH as spectators. As a result, we have extremely high confidence that we have identified the correct configuration and energy for State 1. Thus, we can treat the energy of this state as a fixed, well-established reference.

Moreover, we have discovered a configuration for State 4 with an energy that is only 0.09 eV higher than State 1 at our experimentally observed onset potential (V_{on}). Since the energy of State 1 is fixed, any potential lower-energy State 4 configuration must then have a drop of less than 0.09 eV when transitioning to State 1 at V_{on}. However, this energy drop cannot become negative at V_{on}, as that would inhibit the transition from State 4 to State 1, contradicting experimental results. The lack of options for improvement in energy strongly suggests that any alternative configuration for State 4 would be at most a slight modification of our proposed configuration, perhaps involving some additional, more distant, and thus less relevant spectator species.

Next, we can consider State 3 using the same reasoning as that with State 4. Considering the now-established energy of State 4 and the small 0.16 eV energy drop from State 3 to State 4, there is likewise little room for significant improvement over our identified configuration for State 3. Therefore, any changes to our configuration for State 3 would likely be minor, as well.

Finally, State 2, unlike State 3 and State 4, theoretically could have a new configuration that drops in energy by as much as 0.7 eV without necessarily inhibiting the reaction. In theory, there could exist a qualitatively different State 2 at significantly lower energy than that of our proposed split *H + *(O)(O) configuration. While we cannot definitively rule out this possibility, after a comprehensive search of potential *OO configurations, we found our proposed State 2 as the most energetically favorable and kinetically feasible intermediary between State 1 and State 3. This evidence strongly suggests that we have identified the correct configuration for State 2.

However, even if an improved configuration for State 2 were discovered, our primary conclusion about the significance of split intermediate configurations for the ORR pathway still stands because States 3 and 4 are also both split intermediates. Moreover, the transitions from States 3 to 4 to 1 first become feasible at the correct, experimentally observed onset potential, and the small drops of these transitions imply that they very likely are the rate-limiting steps for the reaction. Consequently, we have high confidence in our identification of the key steps in the alkaline ORR reaction pathway on the $Co_3O_4(100)$ surface.

2.4. Reaction Kinetics. Figure 1 presents the proposed kinetics for our pathway as follows:

1. *H + *OH → * + *(OH)(O): initially, *OH is adsorbed on the Co^{2+} site and a spectator H is adsorbed on one of the four nearby surface O sites. The following motions then occur simultaneously in a coordinated fashion. An O_2 from solution displaces the adsorbed OH, cracks on the Co^{2+} site with one of the O's forming a hydrogen bond with the spectator H, which lifts toward that O (*H + *(O)(O) → * + *(OH)(O)). Meanwhile, the departing OH takes with it an e^- from the electrode to form OH^-.
2. * + *(OH)(O) → * + *(OH)(OH): an H^+ is taken from an H_2O to form a covalent bond with the isolated adsorbed oxygen from the * + *(OH)(O) configuration, leaving an OH^- behind in solution. Meanwhile, the H^+ gathers an e^- from the electrode, forms a covalent bond with the O, and leans over to form an additional hydrogen bond with a nearby surface oxygen atom.
3. * + *(OH)(OH) → *H + *(OH)(OH): an H^+ from an H_2O in solution bonds to a vacant surface oxygen site adjacent to the active Co_{2+} site, absorbing an e^- and leaving an OH^- behind in solution. The newly adsorbed H hydrogen bonds with the O of the nearest adsorbed (OH) fragment.
4. *H + *(OH)(OH) → *H + *OH: finally, one of the attached (OH) groups leaves the surface, bringing the final e^- with it into solution, thereby restoring the original state in the catalytic sequence/cycle.

Similar to ORR on Pt,[23] our pathway features intermediate states like *(O)(O), *(O)(OH), and *(OH)(OH) with split O_2. However, unlike the ORR on Pt, Co_3O_4 utilizes neighboring O sites for hydrogen bonding, suggesting that metal oxides beyond Co_3O_4 may leverage both cations and O sites on the surface to reduce the overall reaction energy in ORR catalysis. We theorize that the proximity and coordination numbers of these cation sites will significantly influence the adoption of a Co_3O_4-like pathway in these metal oxides and likely play a crucial role in their efficiency. Specifically, we theorize that surfaces with easily oxidizable active cations, such as those with low coordination numbers such as the protruding Co^{2+} sites on Co_3O_4, will result in H atoms being shared between adsorbed and surface O sites.

2.5. Impact of Epitaxial Strain. By growing Co_3O_4 as the shell of core−shell nanoparticles, we can induce epitaxial strain and tune the energies of the reaction intermediates to improve the fuel-cell performance. The change in energy per adsorbate $\Delta E^{(a)}$ with epitaxial lattice strain ε_{sys} can be computed from ab initio calculations directly as

$$\Delta E^{(a)} = \Omega \mathrm{tr}([{\sigma_{3d}}^{(a)} - {\sigma_{3d}}^{(0)}]_{2\times2}[\varepsilon_{sys}]_{2\times2}) \tag{4}$$

where $[...]_{2\times2}$ indicates the restriction of a three-dimensional tensor to the two-dimensional space of the plane of the material surface, ${\sigma_{3d}}^{(0)}$ and ${\sigma_{3d}}^{(a)}$ are, respectively, the three-dimensional stress tensors from ab initio periodic supercell calculations of the clean surface and the surface with one adsorbate, and Ω is the volume of the supercell in which the three-dimensional calculations are performed. Defining the adsorbate surface-stress tensor as $s^{(a)} \equiv \Omega[{\sigma_{3d}}^{(a)} - {\sigma_{3d}}^{(0)}]_{2\times2}$, we can write the change in energy per unit area of the surface due to adsorbates as $\Delta E_{ads}/\Delta A = \eta$ tr $s^{(a)}[\varepsilon_{sys}]_{2\times2}$, where η is the density of adsorbates on the surface per unit area, and $s^{(a)}$ is thereby the surface chemical stress tensor associated with the adsorbate.

With the above surface-strain-induced shifts in intermediate state energies, shifts in the onset potential (V_{on}) can also be

Table 1. Predictions of Impact of Epitaxial Strain on Energies of Intermediate States and on the Onset Potential (V_{on}) for Each Case of One of the Reaction Steps Being the Actual Rate-Limiting Step[a]

	intermediate	$dE_k/d\varepsilon$ (meV/%)	rate-limiting step	$dV_{on}/d\varepsilon$ (mV/%)	V_{on} at −1.5% strain (V)	V_{on} at 1.5% strain (V)
1	*H + *OH	−108	1 → 2	−75	1.00	0.78
2	* + *(OH)(O)	−33	2 → 3	18	0.86	0.92
3	* + *(OH)(OH)	−52	3 → 4	26	0.85	0.93
4	*H + *(OH)(OH)	−78	4 → 1	30	0.84	0.94

[a] At present, 3 → 4 and 4 → 1, having the lowest energy drops at V_{on}, appear to be the rate-limiting steps.

expected. To analyze these shifts in V_{on}, we first observed that our identified pathway is sequential without branching. Consequently, the reaction will be switched on and off by whichever step $k \to k+1$ is the rate-limiting step at V_{on}. For a preliminary analysis, we next make the reasonable assumption that, for small shifts in strain, the final net drop in the energy of the rate-limiting step, $E_k - E_{k+1}$, will remain constant at the reaction onset. From the previous paragraph, we have that the application of epitaxial strain ε changes the energy drop between successive states to $E_k - E_{k+1} + \mathrm{tr}(s^{(k)} - s^{(k+1)})\cdot\varepsilon$ so that, to maintain the same final net energy drop, the onset potential must shift by $\Delta V = \mathrm{tr}(s^{(k)} - s^{(k+1)})\cdot\varepsilon/(ne)$, where n is the properly signed number of electrons transferred during the step. Thus, we can expect a rate of change of V_{on} with respect to epitaxial strain of $dV_{on}/d\varepsilon = \mathrm{tr}(s^{(k)} - s^{(k+1)})/(ne)$. Because each reaction step will have a characteristic value for the derivative, by comparing calculated values and experimental measurements of $dV_{on}/d\varepsilon$, one can both confirm that the identified step is present in the actual reaction pathway and determine that it is the rate-limiting step. Thus, through this electrochemical strain spectroscopy (ESS), direct comparisons and identifications can be made between experiments and ab initio calculations.

Table 1 presents our predicted onset potential derivatives $dV_{on}/d\varepsilon$ and predicted V_{on} potentials at −1.5 and 1.5% strain for the case of each reaction step being the possible rate-limiting step for our proposed ORR pathway. Notably, the sign of the strain derivative for the 1 → 2 step is negative, making this the only rate-limiting step that improves with compressive strain. Moreover, the magnitude of the strain derivative for the 2 → 3 step is half that of the 3 → 4 and 4 → 1 steps, making the 2 → 3 step also easy to distinguish from the others.

Finally, from the fact that we have examples of both signs for the onset potential derivative $dV_{on}/d\varepsilon$ with respect to strain, we learn that performance cannot be expected to continue to improve with increasing strain and that there will always be an optimal magnitude for the strain. This is because, regardless of the sign of strain preferred by the rate-limiting step, as the rate-limiting step improves with strain, there are always other reaction steps with derivatives of the opposite sign that therefore become less and less favorable as the magnitude of the strain increases, until one of these steps becomes the rate-limiting step. The optimal strain will then be the point of crossover between the original step and this new step being the actual rate-limiting step.

3. CONCLUSIONS

This work characterizes the oxygen-reduction reaction (ORR) on the (100) surface of cubic Co_3O_4. To explain the experimentally observed onset potential, we performed solvated joint density functional theory (JDFT) calculations by using a detailed computational hydrogen electrode (CHE) method. Our results ultimately led us to propose a new spinel oxide alkaline ORR pathway, which, unlike the pathway typically assumed for metal oxides, exhibits ab initio free energy values in strong agreement with experimental onset potentials for Co_3O_4 cubic nanoparticles. The newly proposed pathway shows PGM-like split (or "cracked") intermediate states in the form *(O)(O), *(O)(OH), and *(OH)(OH), which had not been considered previously for these systems, mediating the reaction by substantially lowering the reaction barrier through hydrogen bonding with induced spectator surface *H atoms on neighboring O sites. This interaction of cation and oxygen sites to produce lower reaction energies likely indicates that other metal oxides use the same mechanisms to catalyze the ORR. Using our novel electrochemical strain spectroscopy (ESS) technique, we also predict the effects of epitaxial strain on the reaction to characterize the strain signature of the limiting step. Having now identified the controlling pathway for ORR on spinel oxides and demonstrated the capability of first-principles calculations to explain the onset potential, the door is now open for the ab initio exploration of the next generation of fuel cell electrocatalysts.

■ ASSOCIATED CONTENT

Supporting Information

The Supporting Information is available free of charge at https://pubs.acs.org/doi/10.1021/jacs.3c11977.

> Ab initio calculation methods: description of DFT calculation parameters and free-energy computation methodology; reaction energy calculations: description of energy terms and calculated values for all species used in free energy computations; and experimental synthesis and electrochemical measurements: description of nanoparticle synthesis and characterization, accompanied by polarization, Tafel, and Koutecký−Levich plots, and electron transfer number determination (PDF)

■ AUTHOR INFORMATION

Corresponding Authors

Colin R. Bundschu − *Department of Applied and Engineering Physics, Cornell University, Ithaca, New York 14853, United States*; orcid.org/0000-0001-7592-9891; Email: crb273@cornell.edu

Héctor D. Abruña − *Department of Chemistry and Chemical Biology, Cornell University, Ithaca, New York 14850, United States*; orcid.org/0000-0002-3948-356X; Email: hda1@cornell.edu

Tomás A. Arias − *Department of Physics, Cornell University, Ithaca, New York 14853, United States*; Email: taa2@cornell.edu

Authors

Mahdi Ahmadi − *Department of Chemistry and Chemical Biology, Cornell University, Ithaca, New York 14850, United States*

Juan F. Méndez-Valderrama − *Department of Physics, Cornell University, Ithaca, New York 14853, United States*

Yao Yang − *Department of Chemistry and Chemical Biology, Cornell University, Ithaca, New York 14850, United States;* Present Address: Department of Chemistry, Miller Institute, University of California, Berkeley, Berkeley, California 94720, United States; orcid.org/0000-0003-0321-3792

Complete contact information is available at: https://pubs.acs.org/10.1021/jacs.3c11977

Notes

The authors declare no competing financial interest.

■ ACKNOWLEDGMENTS

This work was primarily supported by the Center for Alkaline-Based Energy Solutions (CABES), part of the Energy Frontier Research Center (EFRC) program supported by the U.S. Department of Energy, under grant DE-SC-0019445. This work made use of TEM of the Cornell Center for Materials Research Shared Facilities which are supported through the NSF MRSEC program (DMR-1719875). We thank Malcolm (Mick) Thomas at CCMR for help with Nion Ultra STEM. This work was also supported by the Department of Defense (DoD) through the National Defense Science & Engineering Graduate (NDSEG) Fellowship Program. We thank Dr. Kyle Grew of the U.S. Army Research Laboratory for his mentorship throughout the NDSEG program. This work used Jetstream2 at Indiana University through allocation CHE220053 from the Advanced Cyberinfrastructure Coordination Ecosystem: Services & Support (ACCESS) program, which is supported by National Science Foundation grants #2138259, #2138286, #2138307, #2137603, and #2138296.[26]

■ REFERENCES

(1) Stamenkovic, V. R.; Fowler, B.; Mun, B. S.; Wang, G.; Ross, P. N.; Lucas, C. A.; Marković, N. M. Improved Oxygen Reduction Activity on $Pt_3Ni(111)$ via Increased Surface Site Availability. *Science(1979)* **2007**, *315* (5811), 493−497.

(2) Firouzjaie, H. A.; Mustain, W. E. Catalytic Advantages, Challenges, and Priorities in Alkaline Membrane Fuel Cells. *ACS Catal.* **2020**, *10* (1), 225−234.

(3) Ge, X.; Sumboja, A.; Wuu, D.; An, T.; Li, B.; Goh, F. W. T.; Hor, T. S. A.; Zong, Y.; Liu, Z. Oxygen Reduction in Alkaline Media: From Mechanisms to Recent Advances of Catalysts. *ACS Catal.* **2015**, *5* (8), 4643−4667.

(4) Banham, D.; Ye, S. Current Status and Future Development of Catalyst Materials and Catalyst Layers for Proton Exchange Membrane Fuel Cells: An Industrial Perspective. *ACS Energy Lett.* **2017**, *2* (3), 629−638.

(5) Gottesfeld, S.; Dekel, D. R.; Page, M.; Bae, C.; Yan, Y.; Zelenay, P.; Kim, Y. S. Anion Exchange Membrane Fuel Cells: Current Status and Remaining Challenges. *J. Power Sources* **2018**, *375*, 170−184.

(6) Dekel, D. R. Review of Cell Performance in Anion Exchange Membrane Fuel Cells. *J. Power Sources* **2018**, *375*, 158−169.

(7) Chung, H. T.; Cullen, D. A.; Higgins, D.; Sneed, B. T.; Holby, E. F.; More, K. L.; Zelenay, P. Direct Atomic-Level Insight into the Active Sites of a High-Performance PGM-Free ORR Catalyst. *Science* **2017**, *357* (6350), 479−484.

(8) Yang, Y.; Zeng, R.; Xiong, Y.; DiSalvo, F. J.; Abruña, H. D. Cobalt-Based Nitride-Core Oxide-Shell Oxygen Reduction Electrocatalysts. *J. Am. Chem. Soc.* **2019**, *141* (49), 19241−19245.

(9) Yang, Y.; Wang, Y.; Xiong, Y.; Huang, X.; Shen, L.; Huang, R.; Wang, H.; Pastore, J. P.; Yu, S.-H.; Xiao, L.; Brock, J. D.; Zhuang, L.; Abruña, H. D. *In Situ* X-Ray Absorption Spectroscopy of a Synergistic Co−Mn Oxide Catalyst for the Oxygen Reduction Reaction. *J. Am. Chem. Soc.* **2019**, *141* (4), 1463−1466.

(10) Seo, B.; Sa, Y. J.; Woo, J.; Kwon, K.; Park, J.; Shin, T. J.; Jeong, H. Y.; Joo, S. H. Size-Dependent Activity Trends Combined with in Situ X-Ray Absorption Spectroscopy Reveal Insights into Cobalt Oxide/Carbon Nanotube-Catalyzed Bifunctional Oxygen Electrocatalysis. *ACS Catal.* **2016**, *6* (7), 4347−4355.

(11) Suntivich, J.; Gasteiger, H. A.; Yabuuchi, N.; Nakanishi, H.; Goodenough, J. B.; Shao-Horn, Y. Design Principles for Oxygen-Reduction Activity on Perovskite Oxide Catalysts for Fuel Cells and Metal−Air Batteries. *Nat. Chem.* **2011**, *3* (7), 546−550.

(12) Ramaswamy, N.; Tylus, U.; Jia, Q.; Mukerjee, S. Activity Descriptor Identification for Oxygen Reduction on Nonprecious Electrocatalysts: Linking Surface Science to Coordination Chemistry. *J. Am. Chem. Soc.* **2013**, *135* (41), 15443−15449.

(13) Wei, C.; Feng, Z.; Scherer, G. G.; Barber, J.; Shao-Horn, Y.; Xu, Z. J. Cations in Octahedral Sites: A Descriptor for Oxygen Electrocatalysis on Transition-Metal Spinels. *Adv. Mater.* **2017**, *29* (23), No. 1606800.

(14) Li, C.; Han, X.; Cheng, F.; Hu, Y.; Chen, C.; Chen, J. Phase and Composition Controllable Synthesis of Cobalt Manganese Spinel Nanoparticles towards Efficient Oxygen Electrocatalysis. *Nat. Commun.* **2015**, *6* (1), 7345.

(15) Duan, J.; Chen, S.; Dai, S.; Qiao, S. Z. Shape Control of Mn_3O_4 Nanoparticles on Nitrogen-Doped Graphene for Enhanced Oxygen Reduction Activity. *Adv. Funct Mater.* **2014**, *24* (14), 2072−2078.

(16) Gao, R.; Zhu, J.; Xiao, X.; Hu, Z.; Liu, J.; Liu, X. Facet-Dependent Electrocatalytic Performance of Co_3O_4 for Rechargeable Li−O_2 Battery. *J. Phys. Chem. C* **2015**, *119* (9), 4516−4523.

(17) Su, D.; Dou, S.; Wang, G. Single Crystalline Co3O4 Nanocrystals Exposed with Different Crystal Planes for Li-O2 Batteries. *Sci. Rep* **2014**, *4* (1), 5767.

(18) Rong, X.; Kolpak, A. M. Ab Initio Approach for Prediction of Oxide Surface Structure, Stoichiometry, and Electrocatalytic Activity in Aqueous Solution. *J. Phys. Chem. Lett.* **2015**, *6* (9), 1785−1789.

(19) Wang, Y.; Cheng, H.-P. Oxygen Reduction Activity on Perovskite Oxide Surfaces: A Comparative First-Principles Study of $LaMnO_3$, $LaFeO_3$, and $LaCrO_3$. *J. Phys. Chem. C* **2013**, *117* (5), 2106−2112.

(20) Goodenough, J. B.; Cushing, B. L. Oxide-based ORR Catalysts. In *Handbook of Fuel Cells*; Wiley, 2010.

(21) Yang, Y.; Xiong, Y.; Holtz, M. E.; Feng, X.; Zeng, R.; Chen, G.; DiSalvo, F. J.; Muller, D. A.; Abruña, H. D. Octahedral Spinel Electrocatalysts for Alkaline Fuel Cells. *Proc. Natl. Acad. Sci. U. S. A.* **2019**, *116* (49), 24425−24432.

(22) Zasada, F.; Piskorz, W.; Sojka, Z. Cobalt Spinel at Various Redox Conditions: DFT+U Investigations into the Structure and Surface Thermodynamics of the (100) Facet. *J. Phys. Chem. C* **2015**, *119* (33), 19180−19191.

(23) Acres, G. J. K.; Frost, J. C.; Hards, G. A.; Potter, R. J.; Ralph, T. R.; Thompsett, D.; Burstein, G. T.; Hutchings, G. J. Electrocatalysts for Fuel Cells. *Catal. Today* **1997**, *38* (4), 393−400.

(24) Agmon, N. The Grotthuss Mechanism. *Chem. Phys. Lett.* **1995**, *244* (5−6), 456−462.

(25) Momma, K.; Izumi, F. *VESTA 3* for Three-Dimensional Visualization of Crystal, Volumetric and Morphology Data. *J. Appl. Crystallogr.* **2011**, *44* (6), 1272−1276.

(26) Boerner, T. J.; Deems, S.; Furlani, T. R.; Knuth, S. L.; Towns, J. ACCESS: Advancing Innovation. In *Practice and Experience in Advanced Research Computing*; ACM: New York, NY, 2023; pp 173−176.